The Influence of Hydrothermal Synthesis Temperature on the Electronic Structure and Luminescence Property of Cr-Doped $ZnGa_2O_4$ Nanoparticles

Wai-Tung Shiu,[#a] Xincheng Li,[#a] Lo-Yueh Chang,[b] Jeng-Lung Chen,[b] Yung-Yang Lin,[b] Bi-Hsuan Lin,[b] George E. Sterbinsky,[c] Tianpin Wu[c&], John A. McLeod,[d] and Lijia Liu[a*]

[a] Department of Chemistry, Western University, 1151 Richmond Street, London, Ontario, N6A 5B7, Canada
[b] National Synchrotron Radiation Research Centre, 101 Hsin-Ann Road, 30076, Taiwan
[c] Advanced Photon Source, Argonne National Laboratory, 9700 S. Cass Avenue, Argonne, Illinois, 60439, USA
[d] Department of Electrical Engineering, Western University, 1151 Richmond Street, London, Ontario, N6A 5B7 Canada
[#] These authors contributed equally
[&] Present address: Zhejiang University, 866 Yuhangtang Rd, Xihu, Hangzhou, Zhejiang, China, 310027
* Corresponding author email address: Lijia.liu@uwo.ca

Abstract

Cr-doped $ZnGa_2O_4$ (CZGO) is a near-infrared-emitting material with long-lasting persistent luminescence. This unique property makes it a great candidate in optical imaging and sensing for various biomedical applications. Nanosized CZGO can be synthesized via a hydrothermal approach, but the reaction temperatures reported in existing literature vary from 120°C to 220°C, approaching the highest temperature allowed for a standard autoclave vessel. The reason for choosing a particular hydrothermal synthesis temperature has rarely been discussed, and it is unclear whether the resulting CZGO possess the same optical properties. This work compares CZGO nanoparticles synthesized at temperatures from the lowest reported 120°C and to as high as 220°C. We find that although all the synthesized CZGO are light emitting, they exhibit different luminescence intensities and respond differently to the change of excitation energy. X-ray absorption fine structure (XAFS) analysis is employed to investigate the local chemical environment around Zn, Ga and Cr, respectively. We found synthesis temperature strongly influences the Ga species formed in these particles. The energy transfer mechanism is further elucidated using X-ray excited optical luminescence (XEOL) in combination with element-specific XAFS. Two energy transfer paths are identified, which explains the different excitation energy dependencies of the observed photoluminescence.

Keywords
Near-infrared luminescence, $ZnGa_2O_4$, Cr doping, hydrothermal synthesis, X-ray absorption fine structure, X-ray excited optical luminescence

1. Introduction

Zinc gallate ($ZnGa_2O_4$, ZGO) is a ternary oxide compound with a spinel crystal structure. It is a wide band gap semiconductor which emits light in the visible region due to the presence of structural defects (e.g. oxygen vacancies).[1] ZGO is non-toxic and has excellent thermal and mechanical stability. It could serve as the host lattice to accommodate various dopant ions, such as Cr^{3+}, Mn^{2+}, and Eu^{3+}.[2,3] With the presence of dopant ions, ZGO gains unique optical and magnetic properties. Among them, Cr^{3+}-doped ZGO (CZGO) has gained tremendous interest. CZGO emits light in the near-infrared (NIR) region, which comes from the d-d transition of Cr^{3+} in an octahedral environment.[4-6] In addition to this characteristic emission wavelength, Cr-doped zinc gallate (CZGO) has a long decay lifetime, also known as the persistent luminescence (PersL) phenomenon. A recent study by Liu et al. demonstrated that the CZGO nanoparticles made using the hydrothermal method exhibit long-lasting luminescence for up to five days once charged under ultraviolet (UV) light for 10 minutes.[7]

Luminescence in the NIR range has great advantages for a variety of bioapplications. Within the first biological window, light emitting from the luminescent probe has deep tissue penetration depth, allowing for accurate cancer treatment and diagnosis.[7-9] Moreover, materials exhibiting PersL property do not require in-situ excitation, which significantly reduces the autofluorescence emission from body fluids and tissues.[4,7] Minimizing the interference will contribute to a higher signal-to-noise ratio and improve the overall accuracy of diagnosis. For medical applications, CZGO is often used as a luminescent probe in bioimaging.[10,11]

Hydrothermal is a common bottom-up approach to synthesizing CZGO on the nanoscale.[12,13] This synthesis method of CZGO follows a simple metal precursor reprecipitation mechanism. Undoped ZGO can be synthesized under different temperatures, from 100°C to 240°C and it was found that a high synthesis temperature leads to the formation of larger crystals.[13,14] Regarding CZGO, many successful syntheses have been using the hydrothermal method. However, the reported reaction temperatures at which the experiment was conducted vary significantly, from

as low as 120°C, to 220°C being the highest temperature reported. [15-19] It was reported that synthesizing CZGO at different temperatures do not substantially impact the crystalline size, and all nanoparticles are said to have NIR-emission with some extent of PersL. However, the effect of synthesis temperature on the structure of the material has not been investigated. The strength and lifetime of luminescence are highly dependent on the structure of the material.[20] Therefore, conducting an in-depth investigation is necessary to maximize the material's potential.

In this work, CZGO nanoparticles were synthesized at three different temperatures, which are the lowest and highest temperatures reported (120°C and 220°C, respectively),[17, 21] along with an intermediate temperature of 170°C. Although both the luminescent intensity and the PersL lifetime are crucial for bioimaging purposes, our study here will only focus on the luminescent intensity. Using various X-ray spectroscopic techniques to analyze the electronic structure of CZGO, we reveal the correlation between the synthesis temperature and the luminescence properties of the material, which is linked to the electronic structure of CZGO.

2. Materials and Methods

2.1 Materials

Gallium nitrate hydrate ($Ga(NO_3)_3 \cdot xH_2O$, 99.9% trace metals basis), zinc nitrate hexahydrate ($Zn(NO_3)_2 \cdot 6H_2O$, reagent grade, 98%), and ammonium hydroxide solution (NH_4OH, 28 wt%) are obtained from Sigma Aldrich. Chromium nitrate nonahydrate ($Cr(NO_3)_3 \cdot 9H_2O$, 98.5%) and hydrochloric acid (HCl, 36.5-38.0 wt%) are from Alfa Aesar. 2-Propanol is from Fisher Scientific. All the chemicals are analytical grade and used as received.

2.2 Synthesis of Cr-doped $ZnGa_2O_4$

All samples are synthesized using the hydrothermal method based on previously published literature.[7] In two separate vials, 2.5 mmol of $Ga(NO_3)_3 \cdot xH_2O$ and 1.25 mmol of $Zn(NO_3)_2 \cdot 6H_2O$ are dissolved in 5 mL of deionized water separately. The two solutions are then combined under vigorous stirring, and 500 µL of $Cr(NO_3)_3 \cdot 9H_2O$ solution (0.01 mol/L) is added and stirred for 30 minutes. Then, NH_4OH is added dropwise to adjust the pH to 9. A white floccule forms after the target pH is reached. The solution is stirred for an additional 30 minutes. All the above-mentioned steps are performed at room temperature. The solution is then transferred to a 25 mL Teflon-lined autoclave and undergoes hydrothermal treatment for 10 hours at temperatures 120°C, 170°C, and

220°C, respectively. The precipitate is collected by centrifugation at 4500 rpm for 5 minutes. The raw product is washed twice in the order of 5 mL of 0.01 M HCl, and 10 mL of 2-propanol. The final product is obtained by drying in the oven at 60°C for 10 hours. The samples are denoted CZGO-120, CZGO-170, and CZGO-220, respectively, in which the number value marks the hydrothermal synthesis temperature.

2.3 Characterization

The elemental compositions of the samples were analyzed using Energy dispersive X-ray spectroscopy (EDX). The EDX spectrometer is attached to a Scanning Electron Microscope (SEM, LEO (Zeiss) 1540XB FIB/SEM). The energy of the electron beam for EDX analysis was 20 kV. The X-ray diffraction (XRD) was obtained using an Inel XRG3000 generator and an Inel CPS 120 detector with a Cu Kα sealed tube source. The photoluminescence (PL) spectra and photoluminescence excitation (PLE) spectra were collected on a Fluorolog spectrometer (QM-7/2005, Photon Technology Internation (PTI)). The X-ray absorption fine structure (XAFS) spectra were collected at Taiwan Photon Source (TPS), beamline 44A, and Advanced Photon Source (APS), beamline 9-BM. The Zn K-edge and Ga K-edge were collected using the transmission mode, and the Cr K-edge was acquired using the fluorescence mode. The spectra were processed and analyzed using Athena and Artemis from the Demeter software package.[22]

3. Results and Discussions

The crystal structure of the three CZGO nanoparticles synthesized at different hydrothermal temperatures (CZGO-120, CZGO-170, and CZGO-220) is examined by XRD, shown in Figure 1(a). All samples have well-defined diffraction peaks that match the standard diffraction pattern of $ZnGa_2O_4$ (JCPDS 00-038-1240). No impurity phases are observed regardless of synthesis temperature. The peak widths are relatively broad, indicating these CZGO are in the form of nanoparticles. The average crystalline size of each sample is calculated using the Scherrer equation (Equation 1), based on the strongest diffraction peak (311),

$$D = \frac{0.9\lambda}{FWHM \cdot \cos\theta} \qquad (1)$$

where λ is the wavelength of the incident X-ray (1.5406 Å), and FWHM is the full width at half maximum of the (311) peak. The calculated crystalline sizes for CZGO-120, CZGO-170, and

CZGO-220 are 7.07 nm, 8.52 nm, and 10.84 nm, respectively. The trend, plotted in Figure 1(b), is similar to a previous report on an undoped $ZnGa_2O_4$ synthesized using a hydrothermal method.[23] A higher temperature accelerates the conversion of the Ga precursor from GaO(OH) to ultrafine $ZnGa_2O_4$ spinel nuclei, which further facilitates the growth of larger crystals. In fact, hydrothermal synthesis has been used in the past to produce GaO(OH) which is further used to synthesize Ga_2O_3.[24, 25] The synthesis condition, such as the temperature and the type of Ga precursors are very similar to the ones used to synthesize CZGO. Therefore, GaO(OH) may be one of the side or intermediate products during the CZGO formation.

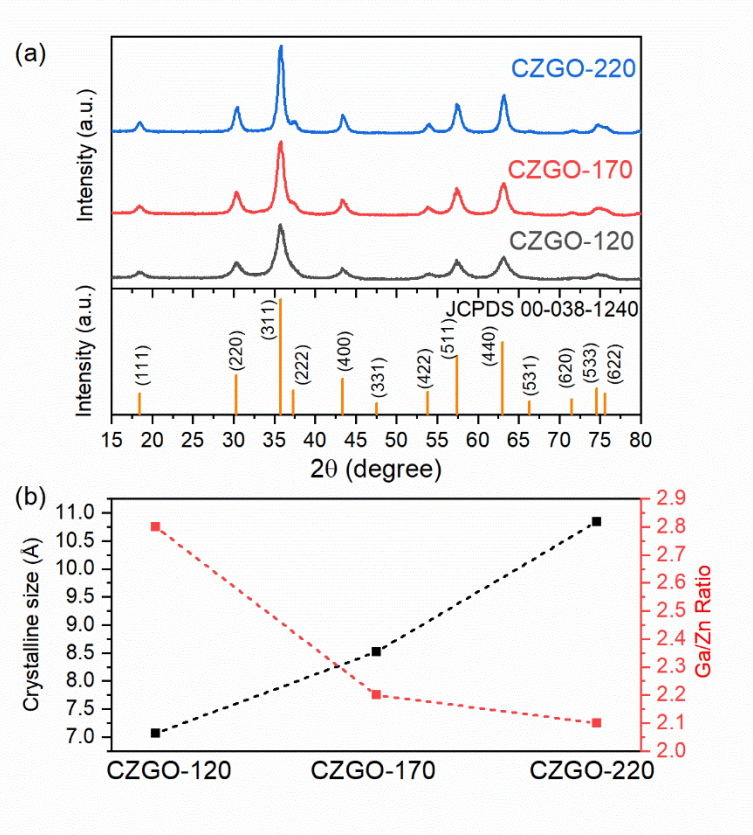

Figure 1. (a) XRD patterns of CZGO synthesized at different temperatures. The standard diffraction of $ZnGa_2O_4$ is included for comparison. (b) The change in the crystalline size and Ga/Zn ratio as a function of temperature.

The elemental compositions of the three CZGO nanoparticles are examined by EDX, and the Ga/Zn ratios are determined by dividing the atomic weight percentages of the two elements. The detailed parameters can be found in the Supporting Information Table S1. Interestingly, although XRD confirms the CZGO nanoparticles all have a ZGO-type crystal structure, the Zn and

Ga concentration in these samples are not at the stoichiometric ratio. At low hydrothermal temperature, the Ga/Zn ratio is at 2.8, indicating insufficient Zn diffusion in the spinel. This value gradually lowers (shown in Figure 1b) with an increased hydrothermal temperature, and finally reaches 2.1 for CZGO-220, which is close to a stoichiometric $ZnGa_2O_4$. Therefore, all CZGO nanoparticles in this study are Zn-deficient. Previous studies also point out that the Zn concentration influences the luminescence properties of Zn.[1,26] For solid-state synthesis, the stoichiometric ratio can be relatively easy to control by tuning the amount of precursor used. In the hydrothermal synthesis, on the other hand, although the Zn and Ga-containing precursor salts were added at the stoichiometric ratio of 1:2, the resulted product is Zn deficient. Many recent works that involve hydrothermally synthesized CZGO use Zn precursor concentration higher than the stoichiometric ratio to the Ga precursor in their synthesis protocol. However, there is no established protocol on the precursor ratio.[7,15,27] The correlation between the precursor ratio and the resulting CZGO stoichiometry requires further study. In this work, we focus on the temperature influence in hydrothermal synthesis. To keep the comparison consistent, the Zn:Ga ratio was kept at 1:2 for all the samples.

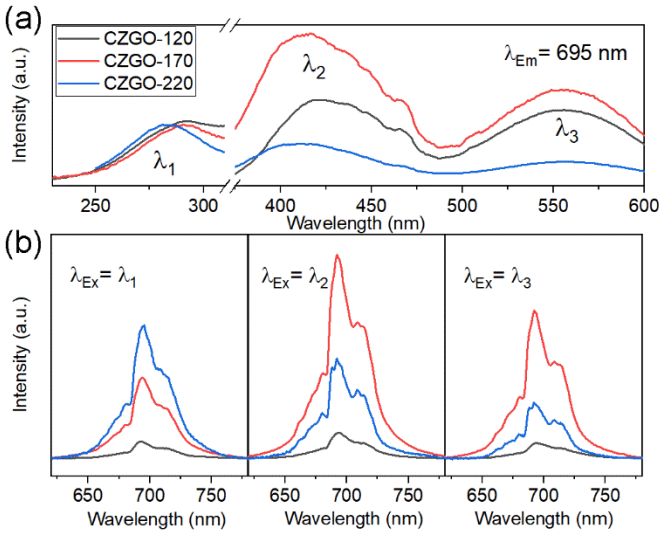

Figure 2. (a) PLE spectra of the three CZGO samples obtained by monitoring the emission at 695 nm. All spectra are normalized to the intensity of the first excitation band (λ_1). (b) PL spectra of CZGO acquired at three excitation wavelengths ($\lambda_1, \lambda_2, \lambda_3$). The exact value of each wavelength is selected based on the location of the PL excitation peak maximum in (a). The color coding is the same as the one used in (a).

The luminescence property of the three CZGO samples is then examined. All samples exhibit characteristic red luminescence from the Cr^{3+} d-d transition under ultraviolet (UV) light excitation. The PL spectra of the three samples exhibit similar profiles that match the characteristic Cr^{3+} d-d transition: the most intense peak at ~700 nm (the N2 line) comes from Cr^{3+} adjacent to an antisite defect (e.g. Zn replaces the Ga site or vice versa), the shoulder at ~688 nm (the zero phonon line, R line) is related to Cr^{3+} in an unperturbed octahedral site, and the remaining features are photon side bands.[28] The photoluminescence excitation (PLE) spectra (Figure 2a) are acquired by monitoring the 695 nm emission to track the energy dependency of the luminescence intensity. All CZGO samples exhibit three PLE bands. The band below 300 nm is the charge transfer band (CTB), which is originated from electrons transferring from the O^{2-} (2p) to Ga^{3+}, Zn^{2+} (4s, 4p).[29] Compared to CZGO-120 and CZGO-170, the peak position of CZGO-220 slightly shifts to a shorter wavelength (282 nm, 4.397 eV). The shift of the CTB has been associated with the change of band gap.[30] Increasing the synthesis temperature likely produces CZGO with larger band gap. It should be noted that the precise determination of the band gap values requires additional characterization. Here we only compare the CTB profile from the PLE spectra to gain a qualitative assessment on the band gap.

The other two PLE bands at ~420 nm (2.95 eV) and ~550 nm (2.25 eV) are from the electronic transition of a Cr^{3+} in an octahedral field ($^4A_2 \rightarrow {}^4T_{1g}$ and $^4A_2 \rightarrow {}^4T_{2g}$, respectively).[31] The energies at which these two transition occurs in the PLE spectrum can be used to determine the crystal field parameter Dq and the Racah parameter B of the Cr^{3+} environment.[30-32] D_q is directly related to the energy of the $^4A_2 \rightarrow {}^4T_{2g}$ transition $E(^4T_{2g})$ by the following equation:

$$D_q = \frac{E(\,^4T_{2g})}{10} \qquad (2)$$

Where the peak maximum of the $^4A_2 \rightarrow {}^4T_2$ transition in the PLE spectra is used to represent the corresponding transitions in the calculation. The Racah parameter B is then derived based on the separation between the $^4A_2 \rightarrow {}^4T_1$ $E(^4T_{1g})$ peak and $^4A_2 \rightarrow {}^4T_2$ $E(^4T_{2g})$ peak in the PLE. However, it is challenging to accurately determine the energy position from a PLE spectrum to represent $E(^4T_{1g})$ and $E(^4T_{2g})$, especially transition into higher energy levels have potential overlaps that further broadening the PLE spectra. Recently, a study proposed a new method of calculating the Racah parameter B using the only $E(^4T_{2g})$ from the PLE spectra and the energy

from the zero phonon line (R line) from the PL emission spectrum ($E_{ZPL,R}$).[33,34] The expression is shown in Equation (3).

$$B = (0.85r + 219)D_q - \frac{1}{2}\left\{\left[(1.69r + 4.39)D_q\right]^2 - 2.22E_{ZPL,R}D_q\right\}^{\frac{1}{2}} \quad (3)$$

Where $E_{ZPL,R}$ refers to the wavelength of the R line in the PL spectra, and r is assumed to be 4.7. In addition, the value of $E(^4T_{2g})$ is derived from a fitting algorithm, instead of the experimentally measured PLE band peak position. A Franck-Condon analysis with the configuration-coordinate model is used to fit the broad $^4A_{2g} \rightarrow {}^4T_{2g}$ transition in the PLE spectrum to obtain the value of the $E(^4T_{2g})$ used in Equation (2).[33] Detailed fitting process can be found in the supporting information. Table 1 lists the crystal field parameters (D_q and B) of the three CZGO samples, and Tanabe-Sugano diagram plot is shown in Figure 3. It can be seen that although the crystal field strength for all CZGO samples are very similar, it is clear that Cr^{3+} in CZGO-170 has the weakest crystal field strength, while the CZGO-220 has the strongest crystal field. This non-linear trend could be further linked to the differences in the energy transfer mechanism which further influences the energy-dependent PL properties.

Table 1. Calculated crystal field parameters of the CZGO samples.

	$E(^4T_{2g})$ (eV)	D_q (cm^{-1})	B (cm^{-1})	D_q/B
CZGO-120	2.068	1668.0	706.7	2.360
CZGO-170	2.065	1665.5	706.6	2.357
CZGO-220	2.073	1672.0	706.7	2.366

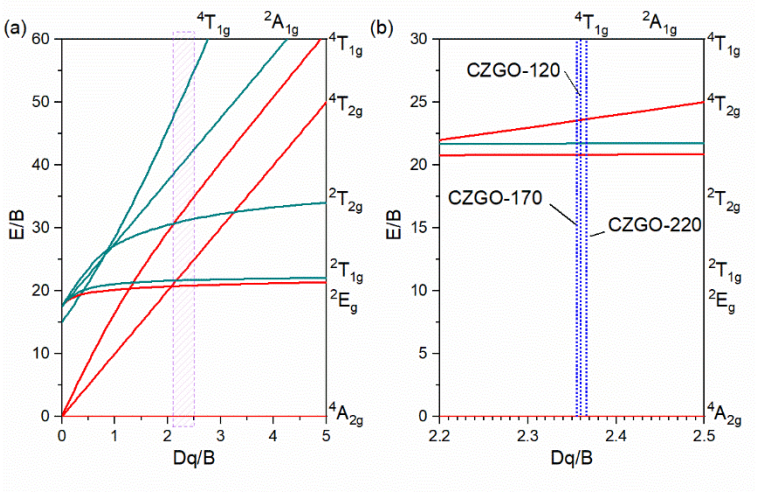

Figure 3. (a) Tanabe-Sugano plot of the Cr^{3+} ion in an octahedral crystal field. The shaded area marks the region where the crystal field parameters of the CZGO nanoparticles are located. (b) A magnified view of the Tanabe-Sugano diagram. The vertical lines mark the parameters calculated for the three CZGO samples.

We next compare the PL intensities of these three samples at different excitation energies. Although quantifying the PL intensity is challenging, the intensities shown in Figure 2 provide a qualitative assessment of the relative PL intensities of these samples under different excitation wavelengths. To do so, each CZGO sample was ground and spread on a double-sided tape. The quantity of samples used and the covered tape area were kept consistent. Spectra were taken using the same instrumentation configuration. Among the three CZGO samples, CZGO-120 has the lowest luminescence intensity regardless of the excitation wavelength. The luminescence profile also lacks fine structure. This could be due to both the poor crystallinity and the Zn/Ga ratio, which has a large deviation from the stoichiometric value. The PL intensities of CZGO-170 and CZGO-220 are comparable but have different excitation-energy dependencies. Under UV light excitation (λ_1 as indicated in Figure 2(a)), CZGO-220 has the strongest emission, while CZGO-170 has a higher emission intensity when excited by visible light (λ_2 and λ_3). This suggests the energy transfer mechanism in CZGO-170 and CZGO-220 is different: luminescence facilitated by charge transfer from the host lattice to the Cr^{3+} is more efficient in CZGO-220, while the dominant luminescence channel for CZGO-170 is through localized excitation of Cr^{3+}. We further examined the PL of CZGO nanoparticles synthesized at two additional temperatures, 145°C and 195°C, respectively. Shown in the Supporting Information Figure S1, the trend of excitation wavelength

dependency is consistent: CZGO synthesized at a high temperature emits strongly under UV (254 nm) excitation, but a high synthesis temperature is not always beneficial for producing strong emission under visible (430 nm) light excitation. Among the five temperatures attempted in this work, CZGO-170 has the brightest emission when excited under 430 nm.

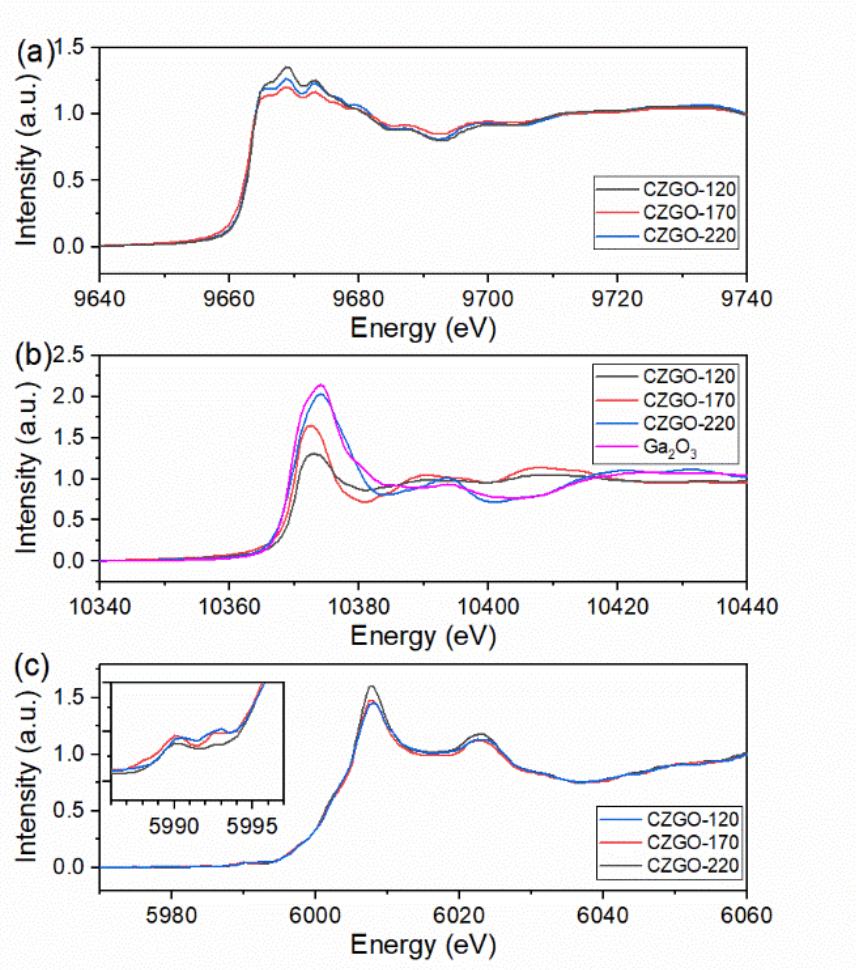

Figure 4. XANES spectra of CZGO synthesized at different temperatures. (a) The Zn K-edge, (b) the Ga K-edge, and (c) the Cr K-edge.

We then investigate the electronic structure of the three CZGO samples by analyzing the X-ray absorption fine structure (XAFS) at the Zn K-, Ga K-, and the Cr K-edge, respectively. Figure 4 shows the X-ray near-edge structure (XANES) of the three samples. The Zn K-edge XANES of the CZGO samples have a similar profile, with small intensity differences at the main resonance (Zn 1s → 4p transition). Features at this region are related to the occupancy of the Zn

4p orbital, which is influenced by the coordination between Zn and its surrounding O neighbors. Due to the hybridization between the two elements, a higher amount of O atoms could facilitate a more efficient charge transfer, hence lowering the 4p electron density (increased absorption peak intensity in the XANES).[35] In our case, the main resonance of CZGO-120 has the highest intensity suggesting CZGO-120 is surrounded by the most O atoms. CZGO-170 has the lowest intensity, therefore it is expected that Zn in CZGO-170 has the least O neighbors (e.g. more oxygen vacancies).

Compared to the Zn K-edge XANES spectra, the differences in the Ga K-edge XANES spectra (Figure 4(b)) are more apparent. The intensities of the main resonance vary and the energy position of the absorption peak maxima of CZGO-220 appears 1.91 eV higher than the remaining samples. The XANES of CZGO-220 shows the highest resemblance of the one of Ga_2O_3. The spectra of CZGO-120 and CZGO-170 have lower whiteline intensities, which means Ga in these two samples are undercoordinated. It is interesting that the Zn K-edge XANES suggests a moderate synthesis temperature (i.e. 170^{o} C) produces Zn of the lowest coordination, but in the case of Ga, CZGO-120 has the lowest Ga-O coordination. This observation is interesting, since the whiteline intensities at the Zn K- and Ga K-edge do not follow the same trend. Quantitative information on the Zn-O and Ga-O bonding will be discussed in the next section with the fitted results from the EXAFS spectra.

The Cr K-edge XANES is shown in Figure 4(c), and a magnified view of the pre-edge region is shown as an inset. Features at this region serve as a better indicator to derive valance states, since it is originated from the dipole-forbidden transition of Cr 1s to 3d states. The shape and intensity of the pre-edge regions reveal the local symmetry where Cr^{3+} sits in the lattice. The overall weak features confirms that Cr^{3+} is in an octahedral coordination, since a tetrahedrally coordinated Cr^{3+} would have a much intense pre-edge peak.[36-38] A close examination reveals that the pre-edge region of the three CZGO sample exhibits a doublet feature. The peak at the higher energy is more noticeable in CZGO-170 and CZGO-120. Previous studies suggested a distorted octahedral environment would exhibit such intensity enhancement.[36] Therefore, increasing the hydrothermal temperature reduces the octahedral distortion of the Cr^{3+}in CZGO.

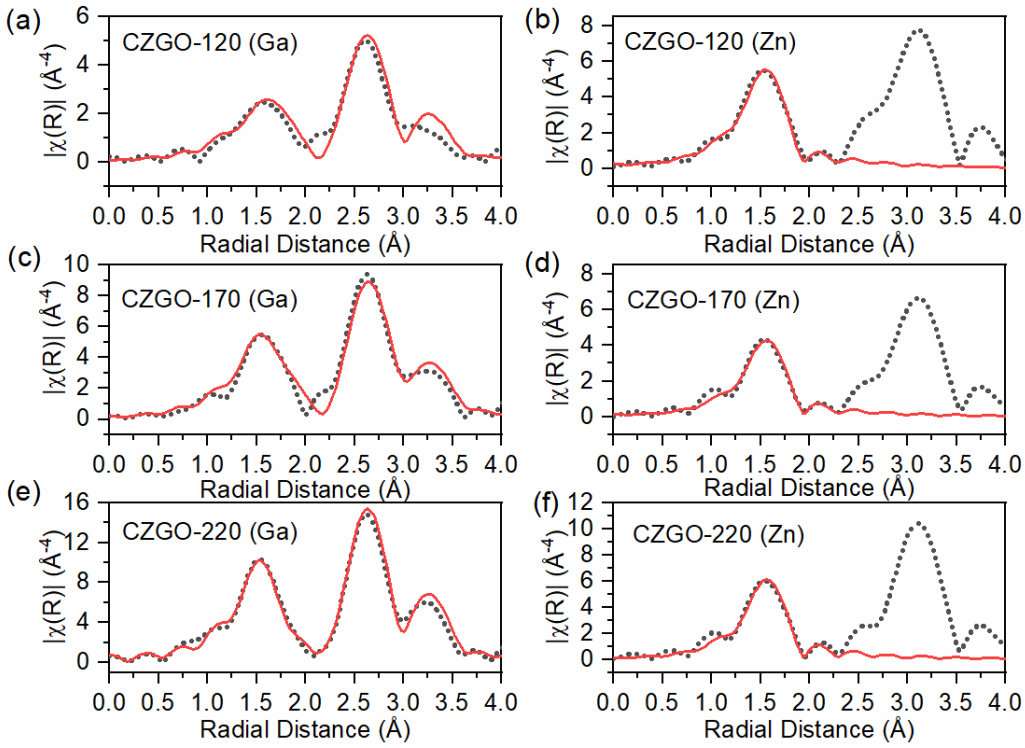

Figure 5. EXAFS spectra at the Zn K- and Ga K-edge for CZGO samples plotted in R-space. (a) Ga K-edge of CZGO-120, (b) Zn K-edge of CZGO-120, (c) Ga K-edge of CZGO-170, (d) Zn K-edge of CZGO-170, (e) Ga K-edge of CZGO-220, (f) Zn K-edge of CZGO-220. In all graphs, the experimental data are displayed in dotted black lines and the fitted spectra are displayed in solid red lines.

Figure 5 shows the Zn K-edge and Ga K-edge EXAFS for CZGO, plotted in Fourier transform magnitudes (i.e. R-space). The spectra were fitted using the normal spinel structure (Fd3m) of $ZnGa_2O_4$. We recognize the presence of antisites in CZGO,[39] but the amount of antisite is much less than the Zn and Ga at the normal sites. The fitted results represent the average coordination environment around Zn and Ga, respectively. The R-space spectra of Zn in $ZnGa_2O_4$ show two main peaks below 3.5 Å. The first peak corresponds to the Zn-O scattering path, the second peak, however, contains three overlapping scattering paths, Zn-Ga, Zn-Zn, and Zn-O, respectively. Since the XANES of the samples at the Zn K-edge (Figure 4a) suggest these samples have a very similar chemical environment around Zn, only the first Zn-O shell is considered in this study. The R-space of Ga in $ZnGa_2O_4$, on the other hand, has three reasonably-well separated peaks. These paths represent the Ga-O, Ga-Ga, and Ga-Zn, respectively. However, when fitting

the EXAFS spectra using these three paths, only CZGO-220 yields a good fit. For CZGO-120 and CZGO-170, another Ga-O path needs to be introduced. This further indicates Ga in CZGO-120 and CZGO-170 has two types of local environment. The complete fitting parameters are summarized in Table 2.

Table 2. EXAFS fitting parameters of CZGO at the Zn K-edge and the Ga K-edge.

	Absorption edge	**Path**	**C.N.**	**R (Å)**	**ΔE (eV)**	**σ^2 (Å^2)**
CZGO-120	Ga K-edge	Ga-O(1)	0.7(5)	1.948(29)	-9.4(1.0)	0.012(5)
		Ga-O(2)	2.0(5)	2.099(11)		0.006(4)
		Ga-Ga	2.0(9)	3.041(10)		0.006(3)
		Ga-Zn	3.3(8)	3.548(19)		0.011(5)
	Zn K-edge	Zn-O	3.8(2)	1.982(7)	0.9(9)	0.007(1)
CZGO-170	Ga K-edge	Ga-O(1)	3.1(1.2)	2.047(44)	-7.1(9)	0.005(4)
		Ga-O(2)	2.6 (1.0)	2.177(57)		0.008(8)
		Ga-Ga	5.2(1.2)	3.052(8)		0.008(3)
		Ga-Zn	4.2(1.5)	3.553 (13)		0.007(4)
	Zn K-edge	Zn-O	2.5(1)	1.980(6)	2.9(8)	0.006(1)
CZGO-220	Ga K-edge	Ga-O	5.8(7)	1.969(4)	-4.8(4)	0.008 (1)
		Ga-Ga	7.0(5)	2.966(5)		0.007(5)
		Ga-Zn	5.2(1.2)	3.480(9)		0.006 (3)
	Zn K-edge	Zn-O	3.2(2)	1.977(7)	3.5(9)	0.005(1)

C.N.: Coordination number, R: radial distance, ΔE: energy shift, σ^2: Debye-Waller factor

To better visualize the influence of synthesis temperature on the coordination number (C.N.) and the interatomic distances around Zn and Ga, Figure 6 is constructed to display these changes as a function of temperature. The horizontal bars in Figures 6(a) and 6(b) mark the corresponding values in a cubic $ZnGa_2O_4$ structure. We first take a look at the Zn local environment. Changing the temperature has minimal effect on the Zn-O bond length. There is only a slight decrease when CZGO is synthesized at a higher temperature. The change is minor, and the values are within the standard deviation of the fitting. The C.N., on the other hand, has a more notable difference. CZGO-120 has the highest C.N. (close to 4), while the C.N. is the lowest in CZGO-170. A high increased synthesis temperature restores the C.N., but Zn is still under-coordinated. If we compare the trend of the energy-dependent PL intensity (Figure 6(c)), we can see that the C.N. of Zn-O follows the trend of the PL under visible light excitation. CZGO-170 has the lowest Zn-O coordination, which gives off the most intense PL under visible light excitation.

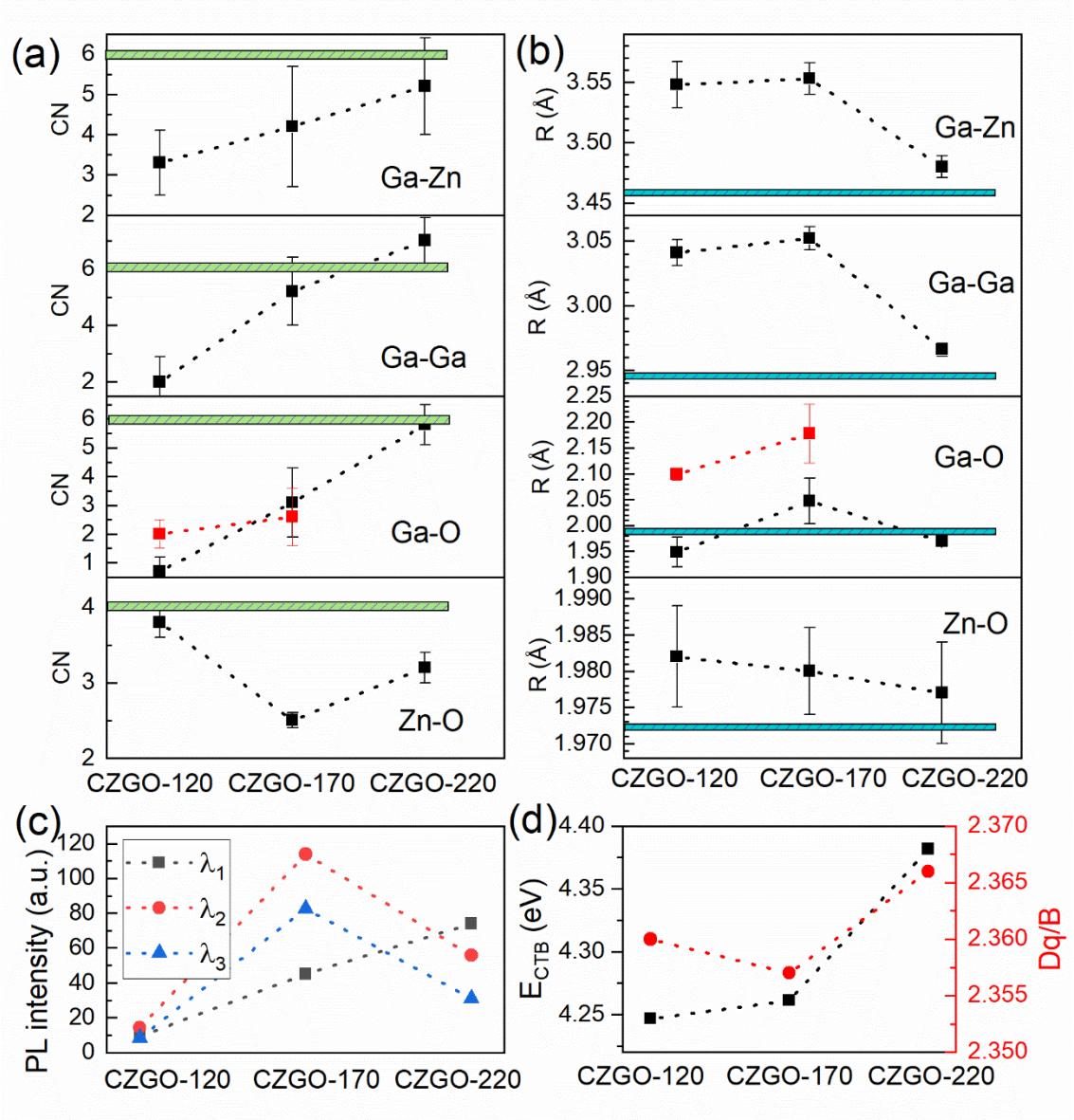

Figure 6. The trend of local coordination environment around the Zn and the Ga centers in the three CZGO samples. The plots are constructed based on the results derived from the EXAFS fitting. (a) The trend of coordination numbers of the Zn and Ga centers, (b) ~~T~~the trend of interatomic distances around the Zn and Ga centers~~.~~, (c) PL intensities of the three CZGO samples under different excitation wavelengths, and (d) comparison of the CTB energy and the crystal field strength (Dq/B) among the three samples.

On the other hand, the Ga coordination environment exhibits a different temperature dependency. Three Ga paths (Ga-O, Ga-Ga, and Ga-Zn) show a consistent trend: the C.N. gradually increases when the synthesis temperature increases. An additional Ga-O only occurs in CZGO-120 and CZGO-170. CZGO-120 has the lowest C.N. (combining the two Ga-O paths), which should be responsible for its lowest PL intensity among the three, regardless of the excitation wavelength. The bond length of Ga-O (as well as the interatomic distances of Ga-Ga and Ga-Zn) exhibits a large variation. In particular, when the synthesis temperature is equal to or below 170ºC, two Ga-O distances are found: one is closer to the Ga-O distance in $ZnGa_2O_4$, and the other is longer, which is similar to one of the Ga-O distances in GaO(OH). GaO(OH) has six O around Ga, which is similar to $ZnGa_2O_4$, however, three of the O in GaO(OH) are further away from Ga. Changing from GaO(OH) to $ZnGa_2O_4$ is expected to have little change on the C. N., but the bond lengths would be more significant. This is consistent with the EXAFS results of CZGO-170 and CZGO-220. Therefore, the hydrothermal synthesis temperature has a more significant impact on the Ga local environment. Ga first forms GaO(OH)-like structure, and Zn diffuses into the lattice, and a high temperature facilitates a complete conversion of $ZnGa_2O_4$. The intermediate GaO(OH) is not at a crystalline phase, since it is not detectable under XRD. EXAFS, however, is sensitive to the local structure and provides evidence on the existence of unique Ga and Zn environments in CZGO-170.

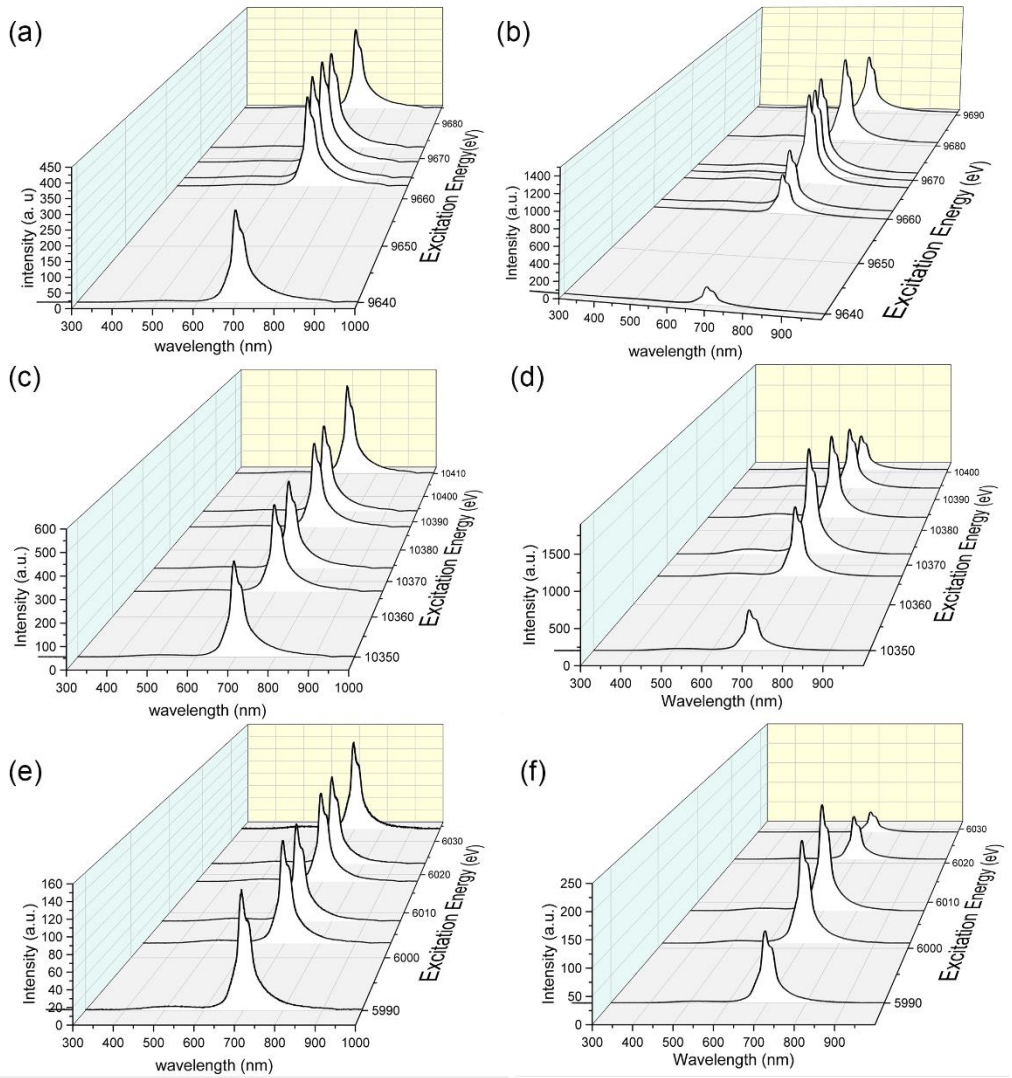

Figure 7. XEOL acquired at selected excitation energies: below and above the Zn K-edge for (a) CZGO-170 and (b) CZGO-220; below and above the Ga K-edge for (c) CZGO-170 and (d) CZGO-220; below and above the Cr K-edge for (e) CZGO-170 and (f) CZGO-220.

Recall the PL of CZGO-170 and CZGO-220, directly promoting the Cr transition channel is more effective in producing luminescence from CZGO-170, while luminescence generated by CZGO-220 favors the host-to-dopant energy transfer mechanism. Figure 6d plots the trend of CTB energy obtained from the PLE spectra in Figure 2 as well as the crystal field strength as a function of the hydrothermal synthesis temperature. We can see the CTB energy has the same trend as the PL intensities excited under UV light, while the PL intensities excited under visible light is correlated with the crystal field strength. We further conducted an energy-dependent XEOL study on CZGO-170 and CZGO-220 to verify the proposed energy transfer mechanism. As shown in

Figure 7, luminescence from CZGO-170 and CZGO-220 are collected by tuning the excitation energies across the absorption edges of the Ga K-, Zn K-, and Cr K-edge, respectively. The luminescence spectra have a similar profile as the ones excited using UV and visible light. Since the excitation event using X-ray is to promote the transition of core electrons, the amount of photons absorbed to promote such transition is directly related to the absorption thresholds of the electron in the element of interest. The luminescent intensity of CZGO-220 clearly shows a strong dependency on the excitation energy: the intensity is weaker below the absorption edge, and the most intensity at the absorption threshold. This means the decay event following the electronic transition goes through a radiative recombination efficiently. The near-band-gap electron-hole pair created upon core electron excitation recombines and transfers its energy to the Cr^{3+} emitting center. On the other hand, the luminescence of CZGO-170 is not energy-dependent. The XEOL intensity remains almost constant before and after a core-electron excitation event. This means the luminescence is not related to the amount of electron-hole pair created near the band gap. Instead, it is induced by energy transfer from defect structure (likely GaO(OH)-related), and which is not specific to a certain electron transition.

4. Conclusions

In summary, although light-emitting CZGO can be synthesized using the hydrothermal method under a wide range of temperatures. The crystalline phase in the final product only contains the cubic spinel $ZnGa_2O_4$ structure. However, our study found that non-crystalline species are present at low and moderate temperatures (i.e. CZGO-120 and CZGO-170). Using XAFS analysis, we identify that the deviation from stoichiometry $ZnGa_2O_4$ is due to an insufficient Zn^{2+} infiltration in to the Ga-O network, and Ga has an intermediate phase of GaO(OH), which fully converts to CZGO at high synthesis temperature. CZGO with and without the additional GaO(OH) have different luminescence mechanisms. Without GaO(OH), CZGO-220 has efficient energy transfer from the near-band-gap excitons to the Cr^{3+}, therefore a higher luminescence intensity is found when using the UV excitation. CZGO-170 favors visible light excitation, as the luminescence doesn't rely on creating near-band-gap excitons, which could be an advantage for creating luminescence using visible light. As CZGO is a known persistent luminescent material, further studies will be conducted to examine how these unique structural features influence the persistent luminescence property of these materials.

Author Contribution

Lijia Liu: conceptualization, supervision, funding acquisition, writing -original draft, writing -review and editing. Xincheng Li: investigation, formal analysis. Wai-Tung Shiu: investigation, formal analysis, writing -original draft, writing -review and editing. Lo-Yueh Chang: investigation. Jeng-Lung Chen: investigation. George Sterbinsky: investigation. Tianpin Wu: investigation. John A. McLeod: formal analysis, writing -review and editing.

Acknowledgements

This work is funded by the Natural Sciences and Engineering Research Council Canada (DG RGPIN-2020-06675 (L.L.) and RGPIN-2022-03871 (J. A. M.). The Taiwan Photon Source is funded by NSRRC. This research used resources of the Advanced Photon Source, a U.S. Department of Energy (DOE) Office of Science user facility operated for the DOE Office of Science by Argonne National Laboratory under Contract No. DE-AC02-06CH11357.

References

1. D. Gourier, A. Bessière, S. K. Sharma, L. Binet, B. Viana, N. Basavaraju, K. R. Priolkar, J. Phys. Chem. Solids 75 (2014) 826-837.
2. P. M. Aneesh, K. M. Krishna, M. K. Jayaraj, J. Electrochem. Soc. 156 (2009) K33 – K36.
3. A. Luchechko, Y. Zhydachevskyy, S. Ubizskii, O. Kravets, A. Popov, U. Rogulis, E. Elsts, E. Bulur, A. Suchocki, Sci. Rep. 9 (2019) 9544
4. S. K. Sharma, D. Gourier, E. Teston, D. Scherman, C. Richard, B. Viana, Opt. Mater. 63 (2017) 51-58.
5. A. Bessiere, B. Jacquart, K. Priolkar, A. Lecointre, B. Viana, D. Gourier, Opt. Express 19, (2011) 10131–10137.
6. P. Dhak, U. K. Gayen, S. Mishra, P. Pramanik, A. Roy, J. Appl. Phys. 106 (2009) 063721.
7. H. Liu, F. Ren, H. Zhang, Y. Han, H. Qin, J. Zeng, Y. Wang, Q. Sun, Z. Li, M. Gao, J. Mater. Chem. B 6 (2018) 1508-1518.
8. R. Pilot, M. Massari, Chem. Phys. Impact 2 (2021) 100014.
9. D. Jaque, C. Jacinto, J. Lumin. 169 (2016) 394-399.
10. X. Sun, L. Song, N. Liu, J. Shi, Y. Zhang, ACS Appl. Nano Mater. 4 (2021) 6497-6514.
11. Z. Xue, X. Li, Y. Li, M. Jiang, H. Liu, S. Zeng, J. Hao, ACS Appl. Mater. Interfaces 9 (2017) 22132-22142.
12. T. Luan, J. Liu, X. Yuan, J. G. Li Nanoscale Res. Lett. 12 (2017) 219.

13. X. Wei, X. Huang, Y. Zeng, L. Jing, W. Tang, X. Li, H. Ning, X. Sun, Y. Yi, M. Gao ACS Nano 14 (2020) 12113–12124.
14. M. Hirano, J. Mater. Chem. 10 (2000) 4690472.
15. Z. Li, Y. Zhang, X. Wu, L. Huang, D. Li, W. Fan, G. Han, J. Am. Chem. Soc. 137 (2015) 5304–5307.
16. T. Maldiney, A. Bessière, J. Seguin, E. Teston, S. K. Sharma, B. Viana, A. J. J. Bos, P. Dorenbos, M. Bessodes, D. Gourier, et al. Nat. Mater. 13 (2014) 418–426.
17. Y. Wang, C. X. Yang, X. P. Yan, Nanoscale 9 (2017) 9049–9055.
18. H. F. Wang, X. Chen, F. Feng, X. Ji, Y. Zhang, Chem. Sci. 9 (2018) 8923–8929.
19. A. Tuerdi, A. Abdukayum, RSC Adv. 9 (2019) 17653–17657.
20. W. T. Shiu, L-Y. Chang, Y. Jiang, M. Shakouri, Y. H. Wu, B. H. Lin, L. Liu, Phys. Chem. Chem. Phys. 24 (2022) 21131-21140.
21. B. B. Sirvastava, S. K. Gupta, Y. Mao, J. Mater. Chem. C. 8 (2020) 6370-6379.
22. B. Ravel, M. Newville, J. Synchrotron Radiation 12 (2005) 537–541
23. M. Hirano, J. Mater. Chem. 10 (1999) 469-472.
24. M. Muruganandhanm, R. Amutha, M. S. M. A. Wahed, B. Ahmmad, Y. Kuroda, R. P. S. Suri, J. J. Wu, M. E. T. Sillanpaa, J. Phys. Chem. C 116 (2012) 44-53
25. Y. C. Zhang, X. Wu, X. Y. Hu, Q. F. Shi, Mater. Lett. 61 (2007) 1497-1499
26. N. Basavaraju, K. R. Priolkar, D. Gourier, S. K. Sharma, A. Bessiere, B. Viana, Phys. Chem. Chem. Phys. 17 (2015) 1790-1799.
27. M. M. Rudolf, G. Bortel, B. G. Márkus, N. Jegenyes, V. Verkhovlyuk, K. Kamarás, F Simon, A. Gali, D. Beke, ACS Appl Nano Mater. 5 (2022) 8950-8961.
28. W. Nie, F. M. Michel-Calendini, C. Linares, G. Boulon, C. Daul, J. Lumin. 46 (1990) 177-190
29. A. Bessière, S. K. Sharma, N. Basavaraju, K. R. Priolkar, L. Binet, B. Viana, A. J. J. Bos, T. Maldiney, C. Richard, D. Scherman, D. Gourier, Chem. Mater. 26 (2014) 1365-1373.
30. Z. Zhang, J. Zhang, Z. Chen, T. Wang, S. Zheng, J. Lumin. 130 (2010) 1738-1743
31. M. Casalboni, A. Luci, U. M. Grassano, B. V. Mill, A. A. Kaminskii, Phys. Rev. B 49 (1995) 3781-3790.
32. W. Dai, F. Chi, B. Lou, X. Wei, J. Cheng, S. Liu, M. Yin, Opt. Mater. 116 (2021) 111104
33. S. Adachi, ECS J. Solid State Sci. Technol. 10 (2021) 026001

34. S. Adachi, ECS J. Solid State Sci. Technol. 9 (2020) 046004
35. C. Guglieri, E. Céspedes, C. Prieto, J. Chaboy, J. Phys.: Condens. Matter. 23 (2011) 206006
36. F. Farges, Phys. Chem. Miner. 36 (2009) 463-481.
37. I. Arcon, B. Mirtic, A. Kodre J. Am. Ceram. Soc. 81 (1998) 222–224.
38. C. Pak, G. L. Haller, Micropor. Mesopor. Mat. 48 (2001) 165–170.
39. N. Basavarju, K. Priolkar, D. Gourier, A. Bessière, B. Viana, Phys. Chem. Chem. Phys. 17 (2015) 10993-10999.